Science Bulletin 62 (2017) 358–368

Contents lists available at ScienceDirect

Science Bulletin

journal homepage: www.elsevier.com/locate/scib

Feature Article

Energy storage materials derived from Prussian blue analogues

Feng Ma [a], Qing Li [a,*], Tanyuan Wang [a], Hanguang Zhang [b], Gang Wu [b,*]

[a] State Key Laboratory of Material Processing and Die & Mould Technology, School of Materials Science and Engineering, Huazhong University of Science and Technology, Wuhan 430074, China
[b] Department of Chemical and Biological Engineering, University at Buffalo, The State University of New York, Buffalo, NY 14260, USA

ARTICLE INFO

Article history:
Received 26 December 2016
Received in revised form 17 January 2017
Accepted 21 January 2017
Available online 14 February 2017

Keywords:
Prussian blue analogues
Energy storage
Rechargeable battery
Open frameworks
Cathode materials
Anode materials
Catalysts

ABSTRACT

Prussian blue analogues (PBAs) with open frameworks have drawn much attention in energy storage fields due to their tridimensional ionic diffusion path, easy preparation, and low cost. This review summarizes the recent progress of using PBAs and their derivatives as energy storage materials in alkali ions, multi-valent ions, and metal-air batteries. The key factors to improve the electrochemical performance of PBAs as cathode materials in rechargeable batteries were firstly discussed. Several approaches for performance enhancement such as controlling the amounts of vacancies and coordinated water, optimizing morphologies, and depositing carbon coating are described in details. Then, we highlighted the significance of their diverse architectures and morphologies in anode materials for lithium/sodium ion batteries. Finally, the applications of Prussian blue derivatives as catalysts in metal-air batteries are also reviewed, providing insights into the origin of favorable morphologies and structures of catalyst for the optimal performance.

1. Introduction

It is of great importance to develop green and sustainable energy storage technologies under the background of excessive depletion of non-renewable fossil fuel and the increasing concerns about global warming. Among various energy storage systems rechargeable lithium-ion batteries (LIBs) that can store electric energy from sustainable resources by electrochemical redox reactions have been most studied, primarily for their high gravimetric capacity and long cycle life [1–7]. After the successful commercialization of LIBs composed of a high-cost $LiCoO_2$ as a cathode material and graphite as an anode material in portable devices in the early 1990s, intensive research has been focused on rechargeable battery technology in order to commercialize it in stationary energy storage and high power density applications such as hybrid electric vehicles (HEVs) and electric vehicles (EVs) [3–5]. However, significant reduction in the cost of LIBs is still required even for mid-sized applications such as HEVs. Thanks to much higher abundance of Fe than Co, $LiFePO_4$ cathode that can be synthesized with cheap raw materials and easy processing procedures have been well studied in recent years [8,9]. However, the poor ionic diffusion caused by the one-dimensional tunnel in $LiFePO_4$'s olivine structure and low electric conductivity make the lithiation/delithiation process too slow to be practically used in EVs and HEVs [10]. Therefore, it is highly desirable to develop advanced lithium hosts with three-dimensional structures for improved Li^+ diffusion/storage. On the other hand, sodium and potassium ion batteries are emerging rechargeable battery forms which have attracted considerable attention due to the low costs and easy accessibility of sodium and potassium [11,12]. Considering their larger ionic size compared with that of Li (e.g., Na (1.02 Å) vs. Li (0.76 Å)), it is even more crucial to search for a host with open framework, high charge storage, and affordable cost for them.

Prussian blue (PB) is an ancient dye invented in the 18th century and can be categorized into soluble PB (generally denoted as $KFe[Fe(CN)_6]$) and insoluble PB (denoted as $Fe_4[Fe(CN)_6]_3$). It is insoluble PB with a chemical formula of $A_xFe[Fe(CN)_6]_y\square_{1-y}{\cdot}mH_2O$ (A: alkali metal; □: $Fe(CN)_6$ vacancy; $0 < x < 2$; $0 < y < 1$) that has been used as electrode materials in both aqueous and organic electrolytes [13–16]. With different amount of alkali element, $A_xFe[Fe(CN)_6]_y\square_{1-y}{\cdot}mH_2O$ can be expressed as Prussian green, Prussian blue, Prussian white, etc. in previous reports [17,18]. Meanwhile, the iron element can be substituted by other transition metals such as manganese [19,20], cobalt [21,22], nickel [23,24], copper [25–27] and zinc [27] without breaking the crystal structure [28,29]. Those varieties make a series of materials with similar chemical compositions and crystal structures to $A_xFe[Fe(CN)_6]_y\square_{1-y}{\cdot}mH_2O$ which are collectively called Prussian blue analogue (PBA) in this paper. In addition, the content of $Fe(CN)_6$

* Corresponding authors.
E-mail addresses: qing_li@hust.edu.cn (Q. Li), gangwu@buffalo.edu (G. Wu).

http://dx.doi.org/10.1016/j.scib.2017.01.030
2095-9273/

vacancy, which generally stem from a rapid precipitation process, is relevant to the amount of coordinated water. Fig. 1 shows the typical face-centered-cubic (fcc) crystal structures of a defect-free PBA (denoted as $A_2M[Fe(CN)_6]$, M refers to transition metal) and a PBA with 25% $Fe(CN)_6$ vacancies (denoted as $A_2M[Fe(CN)_6]_{0.75}\square_{0.25}\cdot mH_2O$) [30]. The high-spin M(II) is octahedrally coordinated with nitrogen in –CN– group while the low-spin Fe (II) is connected to carbon [30,31]. When the $Fe(CN)_6$ vacancy exists, M(II) near the vacancy is prone to coordinate with water molecules, which may lead to lattice distortion and thereby adversely influence the guest cation storage. PBAs with three-dimensional framework are sometimes considered as a kind of MOF (metal organic framework) [32–37], and have large spaces to host cation especially for larger alkali ion such as Na^+ and K^+. When applied in rechargeable batteries, the large channels and interstices in their open framework make PBAs a class of excellent cathode materials with long cycle life and fast charge transfer kinetics. The guest cations (Li^+, Na^+, K^+) are found to be distributed in the nanosized voids of the framework and can diffuse across the cross-sections formed by transition metal and CN ligands. Specifically, compared with another open framework cathode material $Na_3V_2(PO_4)_3$, PBA has a theoretical capacity up to 170 mAh g^{-1} corresponding to two sodium storage, which is higher than that of $Na_3V_2(PO_4)_3$ (117 mAh g^{-1}) [38]. On the other hand, porous or hierarchical materials fabricated using PBAs as templates have been also successfully employed as viable electrode materials for lithium-ion storage [39–42] and metal-air batteries [43–45]. Owing to their low cost, intrinsic open framework and tunable composition, PBAs and their derivatives have great potential to be applied in electrochemical energy storage fields. In this paper, we aim to describe the recent progress of the design and applications of PBAs and its derivatives in energy-related areas.

2. PBA as cathode materials for alkali ion batteries

2.1. Monovalent ion batteries

Lithium intercalation behavior of PB was first studied in an aprotic media [46] and it shows a reversible potential associated with the redox of iron at around 3 V (vs. Li/Li^+). After that a valence tautomeric PBA, i.e., $A_xMn_y[Fe(CN)_6]$ (A = K, Rb), was investigated for the correlations between the type of alkali element and Li^+ insertion/deinsertion behaviors [47]. It was found that in $A_xMn^{II}{}_y[Fe^{III}(CN)_6]\cdot nH_2O$, K or Rb in A sites tended to stabilize the Fe-CN-Mn framework via strong electron delocalization effect and a stable lithium storage was thus obtained. Generally, the vacancy and the associated H_2O are unfavorable to the capacity of rechargeable batteries due to the distorted structure and the hindered ion transfer. As vacancies have great impact on the capacity of PBAs, a vacancy-suppressed PBA framework, MnIII[MnIII$(CN)_6$], was obtained by electrochemical extraction of potassium in a defect-free $K_2Mn[Mn(CN)_6]$ precursor [48]. In the charge/discharge range of 2.0–4.3 V, the obtained $K_{1.72}Mn[Mn(CN)_6]_{0.93}\square_{0.07}\cdot 0.65H_2O$ (□ refers to $[Mn(CN)_6]^{4-}$ vacancies) shows a high lithium storage capacity of 197 mAh g^{-1}, which corresponds to 1.91 lithium insertion per PBA molecule and the energy density per cathode weight is calculated to be 620 Wh kg^{-1}. Unfortunately, the capacity decreases more than 35% after only 10 cycles at a current density of 30 mA g^{-1}. This poor cycling performance is speculated to be originated from the broken of bridging Mn-CN-Mn bonds during the lattice expansion/shrinkage processes which gives rise to possible side reactions. It indicates that the crystal and electronic structure of PBA, which can be adjusted by doping or substitution, are closely related to the cycling capabilities of PBA cathodes. In 2013, trimetallic PBA ($K_{0.1}(Mn_{0.5}Cu_{0.5})[Fe(CN)_6]_{0.7}\cdot 4H_2O$) nanoparticles were applied as cathode materials for Li-ion batteries and revealed a relatively high cycle life of up to 50 cycles with a capacity retention of 75% [49]. The partial substitution of Cu with M significantly suppresses the phase separation induced by over-lithiation and shows better rate performance and stability than bimetallic $K_{0.1}Cu[Fe(CN)_6]_{0.7}\cdot 3.6H_2O$. As the relatively low electric conductivity is also an important factor that restrict the practical usage of PBs/PBAs, conducting polymer has been employed to improve the electric conductivity of PB via an in-situ polymerization coating method [50]. In this system, $Li_3Fe(CN)_6$ acts as not only the precursor of PB synthesis but also the initiator of pyrrole polymerization. The resulting $LiFe^{III}Fe^{II}(CN)_6$-Ppy-PSS (PSS = poly(-sodium 4-styrenesulfonate)), which was added to act as both a surfactant and a dopant during the synthesis) composite cathode exhibits superior cycling stability relative to the bare PB in LIB testing.

A cost-effective alternative for LIBs is sodium ion batteries (SIBs) due to the abundance of sodium relative to lithium. Testing in organic electrolyte, PBAs have the potential to store two Na^+ which corresponds to a capacity of 170 mAh g^{-1}. However, many PBAs only exhibit limited sodium storage and the capacities degrade rapidly [51,52]. This limitation is believed to be associated with $Fe(CN)_6$ vacancies and coordinated water molecules induced during the synthesis, leading to the collapse of cyano-bridged framework and hindering the transportation of Na^+ [30,53–55]. Thus, it is of great importance to eliminating the defects and controlling the coordinated water content. You et al. [53] proposed a

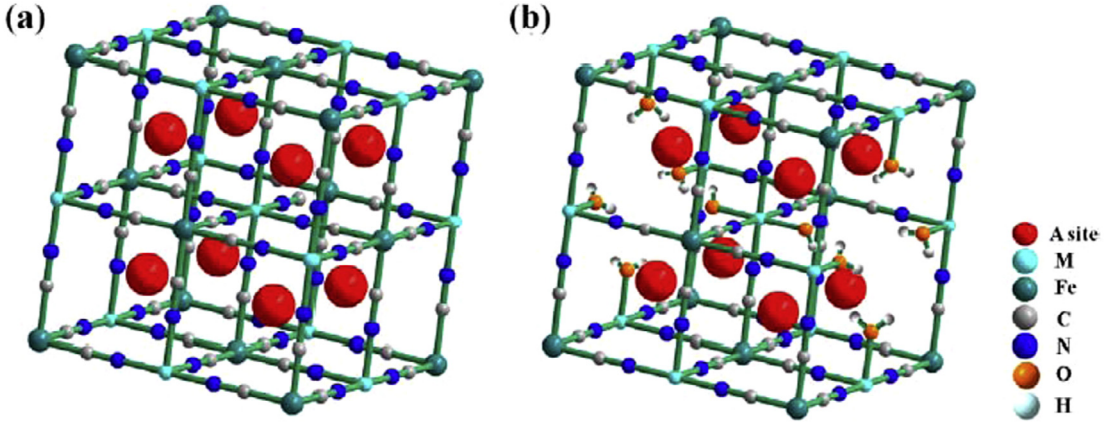

Fig. 1. (Color online) Crystal structure illustrations of (a) a defect-free PBA ($A_2M[Fe(CN)_6]$) and (b) a PBA with 25% vacancies ($A_2M[Fe(CN)_6]_{0.75}\square_{0.25}\cdot mH_2O$) [30]. Adapted and reproduced with permission from Ref. [30] (Copyright 2016 American Chemistry Society).

high quality PB ($Na_{0.61}Fe[Fe(CN)_6]_{0.94}\square_{0.06}$, denoted as HQ-NaFe) with few amounts of vacancies in acid condition using $Na_4Fe(CN)_6$ as the single iron-source precursor. With the assistance of proton, Fe^{2+} was slowly released from $[Fe(CN)_6]^{4-}$ polyanion and subsequently oxidized to Fe^{3+} which reacted with the remaining $[Fe(CN)_6]^{4-}$ to form HQ-NaFe. This preparation method opens a new way to synthesis PBAs. Vacancy and water content in the resulting HQ-NaFe are 6% and 15.7 wt%, respectively, which are much lower than that of low quality PB ($Na_{0.13}Fe[Fe(CN)_6]_{0.68}\square_{0.32}$, denoted as LQ-NaFe) prepared by a conventional precipitation method (32% and 20.7 wt% respectively). This low-defect and water-controlled PB exhibits a high specific capacity of 170 mAh g^{-1} by realizing a two-electron reaction, which is as high as the theoretical capacity of PB (Fig. 2a). With lower polarization between the charge and discharge voltage plateau, HQ-NaFe with fewer vacancies exhibits superior rate capability to that of LQ-NaFe (Fig. 2b). This excellent performance is attributed to the lower charge transfer resistance and higher sodium diffusion coefficient in HQ-NaFe. Coordinated water can be further eliminated by electron exchange between graphene oxide and PB [55]. With the decreasing of crystal water content in the graphene oxide modified PB microcubes, the length of plateau in 3.4 V (vs. Li/Li^+) associated with the oxidation of N-ended Fe (II) in Fe-CN-Fe lattice framework increases from 20 to 60 mAh g^{-1} (Fig. 2c). This observation indicates that lower coordinated water content makes a higher oxidative degree of N-ended Fe(II) in charging process and thus obviously increases the capacity of PB. Low-defect PBA nanocrystals can also be synthesized by a citrate-assisted precipitation method [30]. It can be seen that both citrate-assisted and the blank $Na_2CoFe(CN)_6$ electrodes exhibit two distinguish discharge plateaus at 3.8 and 3.2 V (Fig. 2d), corresponding to the redox reactions of Fe(II) and Co(II) atoms, respectively. However, the citrate-assisted PBA shows a higher capacity (60 mAh g^{-1}) at 3.8 V plateau than that of the blank PBA (28 mAh g^{-1}). This difference in discharge capacity is mainly due to the higher utilization of Fe atoms in citrate-assisted $Na_2CoFe(CN)_6$ which is closely related to reduced $Fe(CN)_6$ vacancies in the PB lattice due to the enriched Na in the case of citrate-assisted sample.

As a cathode material for sodium-ion battery, PBAs with a higher sodium content is regarded to be close to practical use [18,56–61]. As nickel(II) and cobalt(II) ions have a relatively higher antioxidative stability than iron(II) in co-precipitation process, it may be easier for nickel(II) or cobalt(II) hexacyanoferrate (HCF) to form a sodium-rich PB according to the charge balance. Yu et al. [61] studied the correlations between sodium contents and substitution quantities of nickel in the sodium iron-nickel hexacyanoferrate (FeNiHCF). The formula of the as-prepared PBAs were determined as $Na_{0.39}Fe_{0.77}Ni_{0.23}[Fe(CN)_6]_{0.79}\cdot 3.45H_2O$, $Na_{0.324}Fe[Fe(CN)_6]_{0.79}\cdot 4.63H_2O$ and $Na_{1.014}Ni[Fe(CN)_6]_{0.818}\cdot 3.53H_2O$, respectively. It is obvious that the nickel-containing PBAs have higher sodium content and, less defect and water contents than nickel-free PB. When cycling between 2.0 and 4.0 V (vs. Na/Na^+) at a current density of 10 mA g^{-1} the nickel-incorporating PBA shows a capacity retention of 96% after 100 cycles, which is higher than that of nickel-free sample (FeHCF, below 94%). What's more, a higher capacity contribution (48 mAh g^{-1}) of Fe^{2+}/Fe^{3+} redox couple (3.4 V) in NiFeHCF was achieved compared to that of FeHCF (24 mAh g^{-1}). Some antioxidative agents such as ascorbic acid

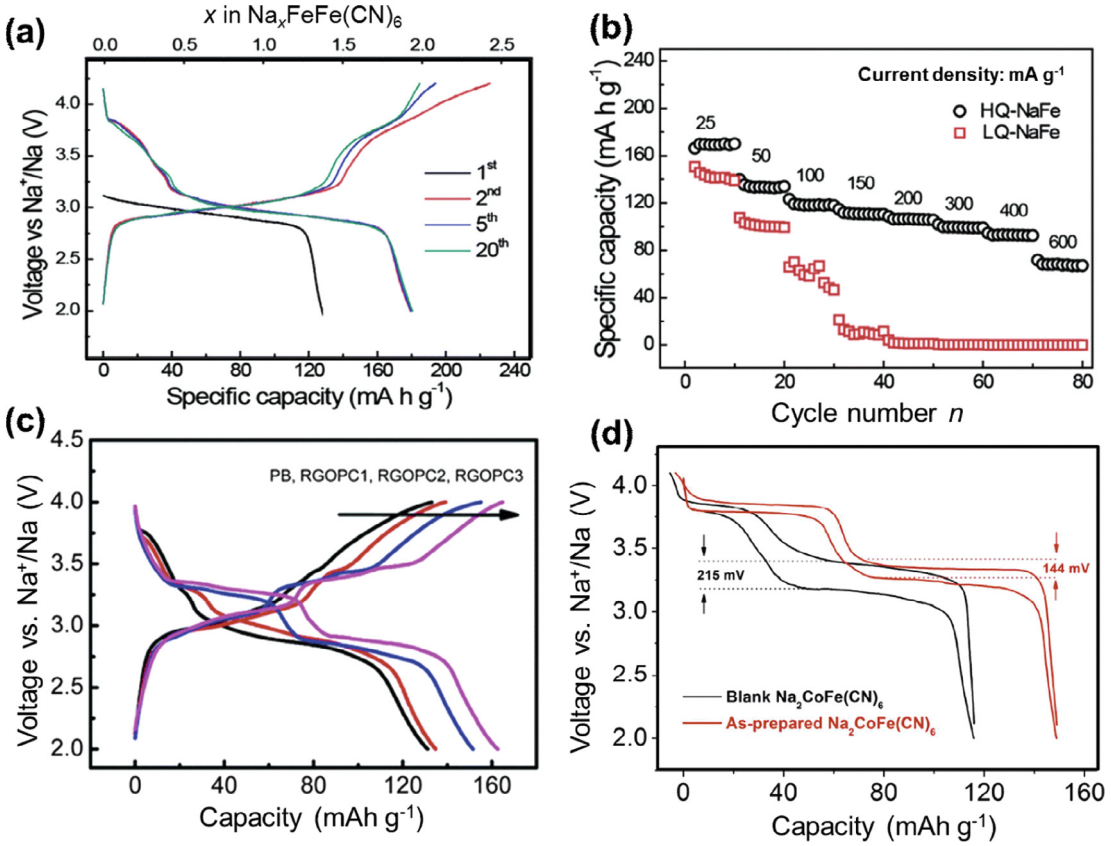

Fig. 2. (Color online) (a) Galvanostatic discharge/charge voltage profiles of HQ-NaFe [53]. (b) Rate capability of HQ-NaFe and LQ-NaFe [53]. (c) The second galvanostatic charge-discharge profiles of PB with different water contents between 2.0 and 4.0 V at 30 mA g^{-1} [55]. (d) Comparison of charge/discharge profiles of blank PBA (black ling) and defect-suppressed PBA (red line) [30]. Adapted and reproduced with permission from Ref. [53] (Copyright 2014 Royal Society of Chemistry), Ref. [55] (Copyright 2016 Royal Society of Chemistry), and Ref. [30] (Copyright 2016 American Chemistry Society).

and citrate can be also used to prepare sodium-rich PBs. Liu and coworkers [58] prepared a sodium-rich PB nanocubes by a facile solution precipitation method at room temperature. $FeCl_2{\cdot}4H_2O$, $Na_4Fe(CN)_6{\cdot}10H_2O$ and sodium citrate are employed as the starting materials and the sodium content in PB can be adjusted by adding different amount of sodium citrate during the synthesis. The obtained Na-rich $Na_{1.70}Fe[Fe(CN)_6]$ shows a capacity as high as 120.7 mAh g^{-1} at 200 mA g^{-1} and an initial coulombic efficiency of 78.3%. When cycling at 1200 mA g^{-1}, the Na-rich PB still maintains a capacity up to 73.6 mAh g^{-1}. Similarly, sodium-rich sample NaFe(1.63) with a chemical formula of $Na_{1.63}FeFe_{0.89}(CN)_6$ was synthesized with the assistance of reducing agent (ascorbic acid) in an inert atmosphere (N_2) [59]. With the scaling up of sodium content, the coulombic efficiency of the first cycle increases gradually. The obtained sodium-rich PB exhibits a discharge capacity of 150 mAh g^{-1}, an excellent cycling performance (90% capacity retention after 200 cycles) and an impressive coulombic efficiency (~100%) as a cathode material of SIB. Inspired by the experimental implications of sodium-rich PBAs, a potassium-rich Prussian White, with a formula of $K_{2-x}Fe_2(CN)_6{\cdot}yH_2O$, was synthesized in comparison with a sodium-containing Prussian White ($Na_{2-x}Fe_2(CN)_6{\cdot}yH_2O$) [18]. It was found that the sodium insertion/deinsertion potential in $K_{2-x}Fe_2(CN)_6{\cdot}yH_2O$ is 0.3 V higher than that in $Na_{2-x}Fe_2(CN)_6{\cdot}yH_2O$. With a bigger radius, the potassium ion in $K_{2-x}Fe_2(CN)_6{\cdot}yH_2O$ stabilizes the framework structure and raises the electrochemical potential of the molecule, resulting in a higher energy density and a more stable cycling performance.

Although the PBAs have open frameworks, introducing extra porosity into the framework of PBAs will further enhance their performance by providing larger channels for facile Na^+ transportation and decreasing diffusion path length, thereby reducing the sluggish solid-state diffusion. Several methods have been used to prepare PBAs with mesoporous morphologies [62–65]. A macro/mesoporous NiHCF was synthesized by a template-free solution method in DMF/H_2O mixed solvent [62]. The macro/mesopores are formed by nanoparticle aggregations and subsequent transformation of interconnected voids to stacked pores. When extending the reaction time from 2 to 72 h, the pore size of NiHCF changes from around 15 nm to more than 45 nm while the Brunauer-Emmett-Teller (BET) surface area decreases from 299 to 93 m^2 g^{-1}. Fig. 3a displays the TEM image of NiHCF obtained after 72 h reaction. Although the capacity of these NiHCF samples are relatively low (less than 70 mAh g^{-1}), the obtained porous/hierarchical structure appears to have positive effect on their rate capabilities. This implication is also confirmed by Zhang et al. [65], which provides a controllable organic-addictive-free etching method to synthesize PBA nanoframes. As shown in Fig. 3b, c, after soaking in acid, the PBA cubes (Fig. 3b) transfers to PBA nanoframes (Fig. 3c) because of the time-dependent preferential etching of proton which breaks down coordination bonds between metal and ligands. With easier access to electrolyte, PBA nanoframes exhibit superior rate capacity and cycling stability to the solid PB cubes (Fig. 3d). Recently, porous $Fe_4[Fe(CN)_6]_3$ sub-micron cubes were reported as a cathode material for SIB [63]. A precipitation method was first used to make solid PB cubes and then the cubes were subject to a PVP-assisted chemical corrosion reaction in acid aqueous solution to obtain porous PB cubes. Fig. 3e illustrates the possible evolution process of material preparation. The porosity is originated from the proton etching of the pristine solid cubes and PVP plays an important role in creating the porosity. In SIB testing, the rate capability of porous PB cubes is much better than that of the solid ones. The capacity of porous PB cubes has a similar capacity with solid ones at low current density (50 mA g^{-1}), while at higher current density (400 mA g^{-1}) the capacity of porous PB cubes is around 75 mAh g^{-1}, which is much higher than that of solid counterparts (c.a. 30 mAh g^{-1}).

The insufficient cycling life is another remaining problem of PBs as cathode materials for sodium-ion battery working in organic electrolyte, especially in low temperature. Carbon nanomaterials such as carbon textiles, carbon black, reduced grapheme oxide (rGO), and carbon nanotube (CNT) with the advantage of low cost, easy preparation, and high electronic conductivity may solve the problems originated from the structural imperfection and low conductivity of PBs by providing a high conductive scaffold and preventing the undesirable exfoliation of active materials [55,66–69]. Flexible $Fe[Fe(CN)_6]$/carbon cloth composites are synthesized by an in-situ precipitation strategy and utilized as a binder free host for sodium ion insertion [66]. Fig. 4a displays the SEM image of the $Fe[Fe(CN)_6]$/carbon textiles. The carbon fibers keep the ordered woven structure of the carbon cloth after the crystal growth of $Fe[Fe(CN)_6]$, but exhibit a rougher surface as compared to that of the pure carbon cloth. With the help of the intimate connected carbon matrix, the flexible electrode displays a long term cycling life with 81.2% capacity retention over 1000 cycles. PB/C composite was prepared by dispersing Ketjen black in acidic solution of $Na_4Fe(CN)_6{\cdot}10H_2O$ and a subsequent heating treatment [68]. PB cubes decomposing from $Na_4Fe(CN)_6$ were formed on Ketjen black particles. After working at a current density of 2000 mA g^{-1} for 2000 charge/discharge cycles, the PB/C can still maintain 90% of its original capacity (Fig. 4b). This excellent stability should be attributed to the fact that small size and intimate contact of the PB cubes with the carbon matrix assure both a shortened Na-ion diffusion length and fast electron transfer within the electrode. First-principle calculations suggest that the PB/C with low defect content has a higher electrochemical activity should be due to the carbon-ended Fe(II) (the low spin Fe) and thus has a higher capacity in contrast to the bare PB. In order to improve the electrochemical performance of PB at low temperature, CNTs were imposed to cross link with PB and a conductive network was formed [69]. The addition of CNTs doesnot change the morphology and chemical structure of cubic-shaped PB. In fact, they embed into the PB cubes and linked monodisperse PB cubes together (Fig. 4c). By this way the contact resistance between PB particles is significantly alleviated and rate capacity as well as the low temperature performance are greatly improved (Fig. 4d). Even the working temperature is as low as −25 °C, the PB/CNT cathode can deliver a discharge capacity of 142 mAh g^{-1}, which corresponds to an output specific energy density of 408 Wh kg^{-1} and a 86% capacity retention after 1000 cycles at 2.4 C.

When switching organic electrolytes to aqueous ones, the capacity of a SIB would typically decrease due to the relatively narrow electrochemical window of aqueous solution. However, aqueous SIBs have the advantages of low cost and inherent safety, and thus are particularly suitable for large-scale energy-storage applications. Therefore, it is also beneficial to choose PBAs with open framework as sodium hosts in aqueous sodium-ion battery. Early works on sodium intercalation in PBAs are usually based on thin electrodeposited films with thicknesses of approximately 100 nm, which is too thin for practical use. Cui and coworkers [70,71] reported a series of nanoparticulate materials with the PB structure (such as CuHCF, NiHCF and $Cu_{0.56}Ni_{0.44}HCF$) and studied their electrochemical performance in aqueous electrolyte. In 1 mol L^{-1} $NaNO_3$ aqueous electrolyte the average discharge potential of the PBAs changes from 0.75 V (vs. saturated calomel electrode, SCE) of NiHCF to 0.92 V of CuHCF [71] (Fig. 5a) which should be ascribed to the higher redox potential of Cu(II)/Cu(III) than Ni(II)/Ni(III). In spite of their relatively low capacity (around 56 mAh g^{-1}), NiHCF and $Cu_{0.56}Ni_{0.44}HCF$ have good cycling stability and show no capacity degradation after 2000 cycles at 500 mA g^{-1} (Fig. 5b). In order to break the capacity limitation of previously studied PBAs in aqueous electrolyte (about 60 mAh g^{-1}), vanadium HCF was proposed as a novel cathode material for aqueous rechargeable battery

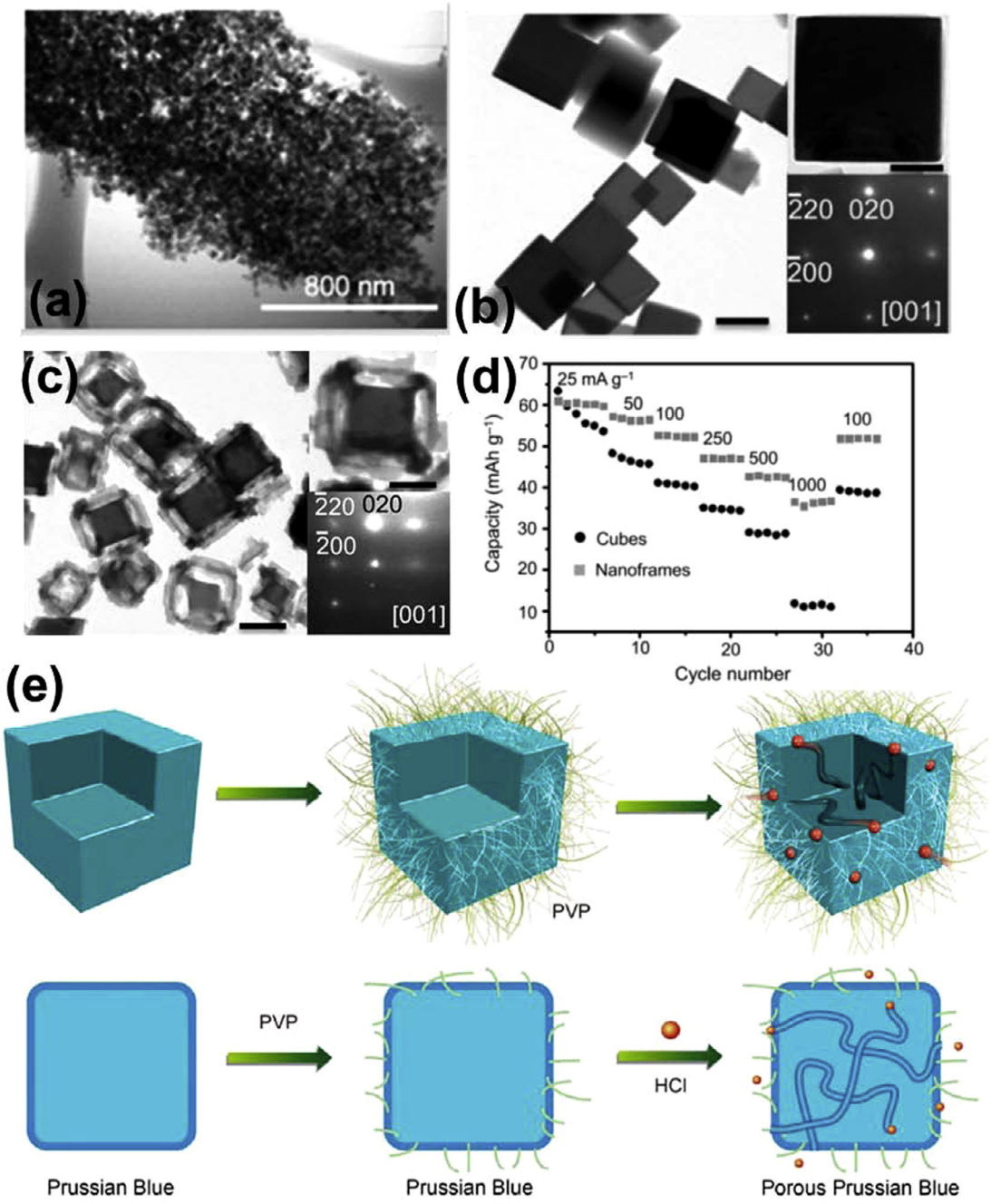

Fig. 3. (Color online) (a) TEM image of porous NiHCF obtained after 72 h reaction [62]. (b) TEM of NiFe(II) PBA cubes [65]. (c) TEM of NiFe(II) PBA nanoframes [65]. (d) Rate performance of PBA cube and PBA nanoframe as cathodes for SIBs [65]. (e) Schematic illustration of the synthesis process of porous PB submicron cubes and the role of PVP [63]. Adapted and reproduced with permission from Ref. [62] (Copyright 2014 Wiley-VCH), Ref. [65] (Copyright 2016 Wiley-VCH), and Ref. [63] (Copyright 2016 American Chemistry Society).

[72]. The V/Fe PBAs were synthesized by a co-precipitation method in acid environment with VCl_2 and $Na_4Fe(CN)_6{\cdot}10H_2O$ as starting materials. The V/Fe PBAs delivered a high discharge capacity of c. a. 90 mAh g^{-1} (Fig. 5c) in the range of 0.4–1.2 V (vs. Ag/AgCl) under a current density of 55 mA g^{-1} (around 1.2 C) and exhibited high recycling efficiency, which was greatly enhanced compared to that of Cu/Fe and Ni/Fe PBAs. Such great improvement may be attributed to 3D network of hydrogen bonding and the larger lattice parameter resulted from the introduction of vanadium, which leads to a faster diffusion kinetics and lower activation energy for charge transfer process. Recently, vacancy-free $Na_2CoFe(CN)_6$ nanocubes was synthesized by a controlled crystallization reaction with the assistance of a structure-directing agent (sodium citrate) [73]. The synergistic effect of Fe^{2+}/Fe^{3+} (0.9 V) and Co^{2+}/Co^{3+} (0.4 V) redox couples brings about a remarkable high reversible capacity of 130 mAh g^{-1} (Fig. 5d) in the potential range of 0–1.1 V (vs. Ag/AgCl). This result implies that in aqueous electrolyte the Co^{2+}/Co^{3+} couple may be favorable to capacity enhancement among the transition metal redox couples of PBAs.

2.2. Multivalent ion batteries

Multivalent ion (such as Mg, Ca, Al) battery is considered to potentially surpass LIB and can be employed as the next generation

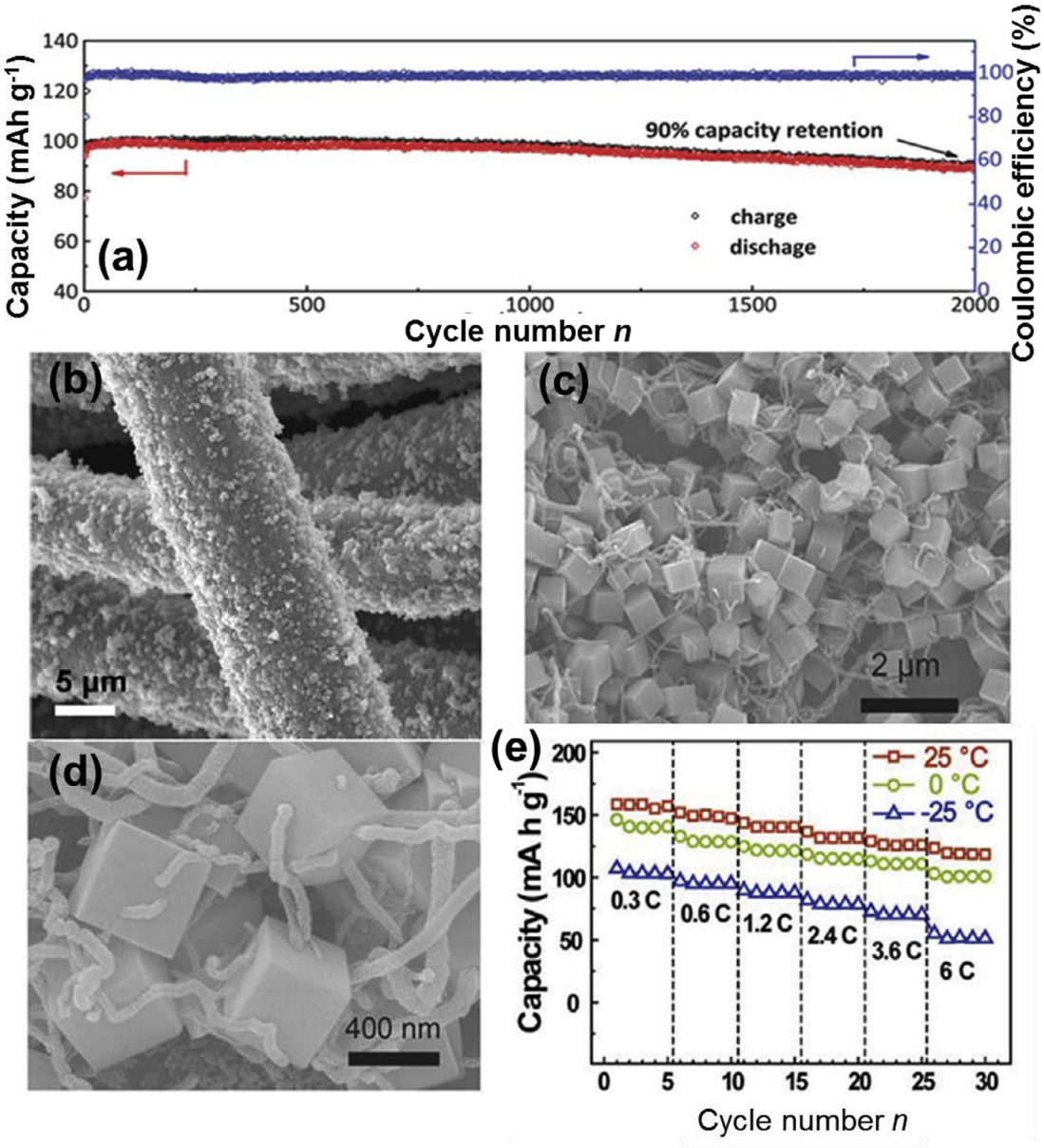

Fig. 4. (Color online) (a) Cycling performance of PB/C at a current density of 2000 mA g^{-1} (20 C) [68]. (b) SEM images of the $Fe[Fe(CN)_6]$/carbon textiles [66]. (c, d) SEM images of the PB/CNT with different magnification [69]. (e) Rate capabilities of the PB/CNT working at different temperatures [69]. Adapted and reproduced with permission from Ref. [66] (Copyright 2015 Royal Society of Chemistry), Ref. [69] (Copyright 2016 Wiley-VCH), and Ref. [59] (Copyright 2016 Wiley-VCH).

energy storage system. However, the insertion/deinsertion of multivalent ions in host frameworks has proved to be difficult because of the increased electrostatic interaction between multivalent positive ions and negative atoms. The increased charge concentration would lead to sluggish kinetics of charge transfer and poor cyclability. Thanks to large tunnels and open frameworks for ion transport, PBAs have the priority to serve as cathode materials for those multivalent ion batteries and have been intensively studied in recent years [25,74–83]. The insertion behaviors of alkali earth metal cations (Mg^{2+}, Ca^{2+}, Sr^{2+}, Ba^{2+}) in a nanoscale NiHCF electrode in aqueous solution have been systematically investigated by Wang et al. [74]. Their study implies that the NiHCF can indeed react with divalent ions reversibly to perform considerable cycling numbers. Later the same group reported the reversible insertion of several trivalent ions such as Y^{3+}, Nd^{3+}, Ce^{3+}, La^{3+}, Sm^{3+} into nanosized CuHCF [75]. This study demonstrates that unlike previous studies of sodium storage behavior [53–55] in PB, the $Fe(CN)_6$ defects and coordinated water have positive effects on the insertion/deinsertion kinetics of multivalent ions to some extent. The defect provides the cation diffusion path and the coordinated water is able to reduce the electrostatic repulsion which in turn decreases the activation energy of interfacial charge transfer in charge/discharge cycles. Zinc ion secondary battery with a metallic zinc as anode and a nanostructured PBA as cathode was studied by Liu et al. [76]. The cell exhibits a well-defined discharge voltage plateau of around 1.1 V with a specific capacity of about 120 mAh g^{-1} at a current of 10 mA g^{-1}. Recently, a sodium containing PB ($Na_{0.69}Fe_2(CN)_6$) was synthesized as a high-voltage cathode material for magnesium batteries with 1 mol L^{-1} $Mg(TFSI)_2$/AN as electrolyte [77]. It is found that the $Na_{0.69}Fe_2(CN)_6$ shows reversible intercalation/deintercalation of Mg^{2+} while Mg^{2+} cannot be intercalated in Na-free $Fe_2(CN)_6$, indicating Na^+ in $Na_{0.69}Fe_2(CN)_6$ plays a crucial role in stabilizing Mg^{2+}. In Mg ion battery testing, $Na_{0.69}Fe_2(CN)_6$ delivers reversible capacity of approximately

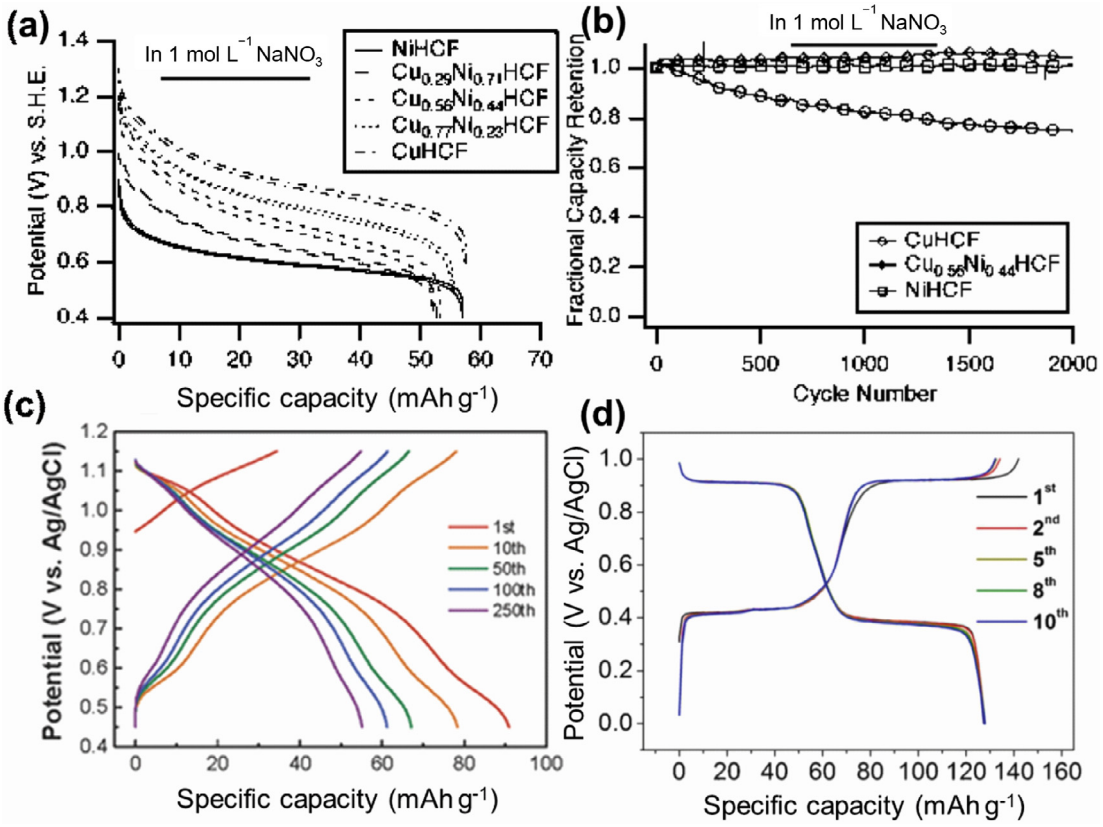

Fig. 5. (Color online) (a) Potential profiles of CuHCF, NiHCF, and CuNiHCF during galvanostatic cycling in 1 mol L^{-1} $NaNO_3$ [71]. (b) Cycling data of CuHCF, NiHCF, and CuNiHCF at 500 mA g^{-1} [71]. (c) Potential profiles of the cathodes synthesized by co-precipitation (with HCl), evolving over 250 cycles (potential range: 0.45–1.15 V vs Ag/AgCl, charge/discharge current density: 110 mA g^{-1}) [72]. (d) Charge/discharge profiles of $Na_2CoFe(CN)_6$ in aqueous media at a current density of 130 mA g^{-1} [73]. Adapted and reproduced with permission from Ref. [71] (Copyright 2012 American Chemistry Society), Ref. [72] (Copyright 2016 Wiley-VCH), and Ref. [73] (Copyright 2015 Wiley-VCH).

70 mAh g^{-1} at 3.0 V (vs Mg/Mg^{2+}) and shows stable cycle performance over 35 cycles. Besides, Tohru Shiga's group [78] observed the first electrochemical insertion of Ca^{2+} into PBA, $MnFe(CN)_6$, in nonaqueous solutions of $Ca(CF_3SO_3)_2$ and various solvents including ionic liquid at 60 °C. The cell delivers an initial discharge capacity of about 70 mAh g^{-1} while it decreases rapidly within 20 cycles. Despite those reports on PBAs as multivalent ion hosts, their obtained capacity is still limited (no more than 100 mAh g^{-1}) until now and further improvement in the cycling stability is required. For the latter one, electing a suitable electrolyte may be a key factor. Overall, the applications of PBA in multivalent ion batteries with nonaqueous electrolyte is a promising area but still requires further research.

In order to better understand the progress of using PBAs in energy storage area, a table summarizing the performance of PBAs as cathode materials for secondary ion batteries in recent publications is presented in Table 1.

3. PBA and PBA derivatives as anode materials for lithium/sodium ion batteries

PBAs with open frameworks and rich active sites can be also employed as anode materials for lithium/sodium ion batteries. Several works have been done to explore the lithium storage behaviors of PB as an anode material in LIBs [42,84,85]. $Co_3[Co(CN)_6]_2$ and $Mn_3[Co(CN)_6]_2$ were synthesized by a surfactant-assisted precipitation method and directly used as anode materials for LIBs [42]. The reversible capacities of $Co_3[Co(CN)_6]_2{\cdot}nH_2O$ at 20 mA g^{-1} are measured to be 294.2 mAh g^{-1} and the average working potential is about 1.5 V (vs. Li/Li^+). Similar results were obtained by a potassium-containing PB which has a reversible capacity up to 450 mAh g^{-1} at 8.75 mA g^{-1} [84].

Limited by the relatively low capacity of PB, transition metal oxides derived from different structured PBs as the self-template were intensively studied [34–36,39–41,86–94]. Co_3O_4 nanocages were synthesized by simply annealing as-synthesized $Co_3[Co(CN)_6]_2$ in air at 400–600 °C [86,87]. Kirkendall effect in the calcination leads to the porous and hierarchical structure of the obtained Co_3O_4. Similar approach has also been used to synthesize porous Fe_2O_3 nanocubes [35], $ZnCo_2O_4$ microsphere [93], porous $ZnO/ZnFe_2O_4$ composite [94] and other bimetallic oxides [36,39,89]. Zhang and coworkers [40] produced hierarchical Fe_2O_3 microboxes by controlling the sintering temperature of PB. When the annealing temperature was 650 °C, hierarchical microboxes constructed of Fe_2O_3 nanoplatelets were produced. Surface treatments of PB precursors by hetero-atoms before calcination in air can lead to a hollow or hierarchical multi-component metal oxides [34,41,88,92] because of the enhanced Kirkendall effect. A general and simple approach for large-scale synthesis of porous hollow spinel AFe_2O_4 (A = Zn, Ni, Co) nanoarchitectures via PB self-sacrificial template strategy is proposed by Yu et al. [34]. During the calcination process the absorbed hetero cations such as Zn^{2+}, Ni^{2+}, Co^{2+} react with oxygen to form a shell of AFe_2O_4 while Fe atoms in the inner PB diffuse outward by the concentration gradient which eventually leads to a hollow AFe_2O_4. The hollow

Table 1
Representative performance of secondary ion batteries using PBAs as cathodes.

Samples	Rate capacity	Capacity retention	Ion	Refs.
$K_{0.1}(Mn_{0.5}Cu_{0.5})[Fe(CN)_6]_{0.7}\square_{0.3}$ nanoparticles	94 mAh g^{-1} at 30 mA g^{-1} 38 mAh g^{-1} at 1000 mA g^{-1}	74.5% after 50 cycles (30 mA g^{-1})	Li^+	[49]
$LiFeFe(CN)_6$-Ppy-PSS hybrid	120 mAh g^{-1} at 20 mA g^{-1} 50 mAh g^{-1} at 373.6 mA g^{-1}	>80% after 200 cycles (20 mA g^{-1})	Li^+	[50]
$Na_2CoFe(CN)_6$ nanocrystals	148 mAh g^{-1} at 20 mA g^{-1} 60 mAh g^{-1} at 500 mA g^{-1}	90% after 200 cycles (100 mA g^{-1})	Na^+	[31]
$Na_{0.61}Fe[Fe(CN)_6]_{0.94}$ cubes	170 mAh g^{-1} at 25 mA g^{-1} 70 mAh g^{-1} at 600 mA g^{-1}	98% after 150 cycles (25 mA g^{-1})	Na^+	[53]
$FeFe(CN)_6$/carbon cloth	80 mAh g^{-1} at 24 mA g^{-1} 58 mAh g^{-1} at 1200 mA g^{-1}	75% after 200 cycles (60 mA g^{-1}) 81.2% after 1000 cycles (120 mA g^{-1})	Na^+	[66]
$Na_{0.647}Fe[Fe(CN)_6]_{0.93}$ $2.6H_2O$@C	130 mAh g^{-1} at 50 mA g^{-1} 77.5 mAh g^{-1} at 9000 mA g^{-1}	90% after 2000 cycles (2000 mA g^{-1})	Na^+	[68]
Prussian blue/CNT	167 mAh g^{-1} at 0.1 C 125 mAh g^{-1} at 6 C	86% after 1000 cycles (2.4 C)	Na^+	[69]
$K_{0.220}Fe[Fe(CN)_6]_{0.805}\square_{0.195}\cdot 4.01H_2O$ nanoparticles	65 mAh g^{-1} at 100 mA g^{-1} 50 mAh g^{-1} at 400 mA g^{-1}	86.5% after 150 cycles (200 mA g^{-1})	K^+	[12]
$K_{0.03}Cu[Fe(CN)_6]_{0.65}\cdot 2.6H_2O$ nanoparticles	65 mAh g^{-1} at 0.2 C 55 mAh g^{-1} at 10 C	80% after 2000 cycles (5 C)	Pb^{2+}	[75]

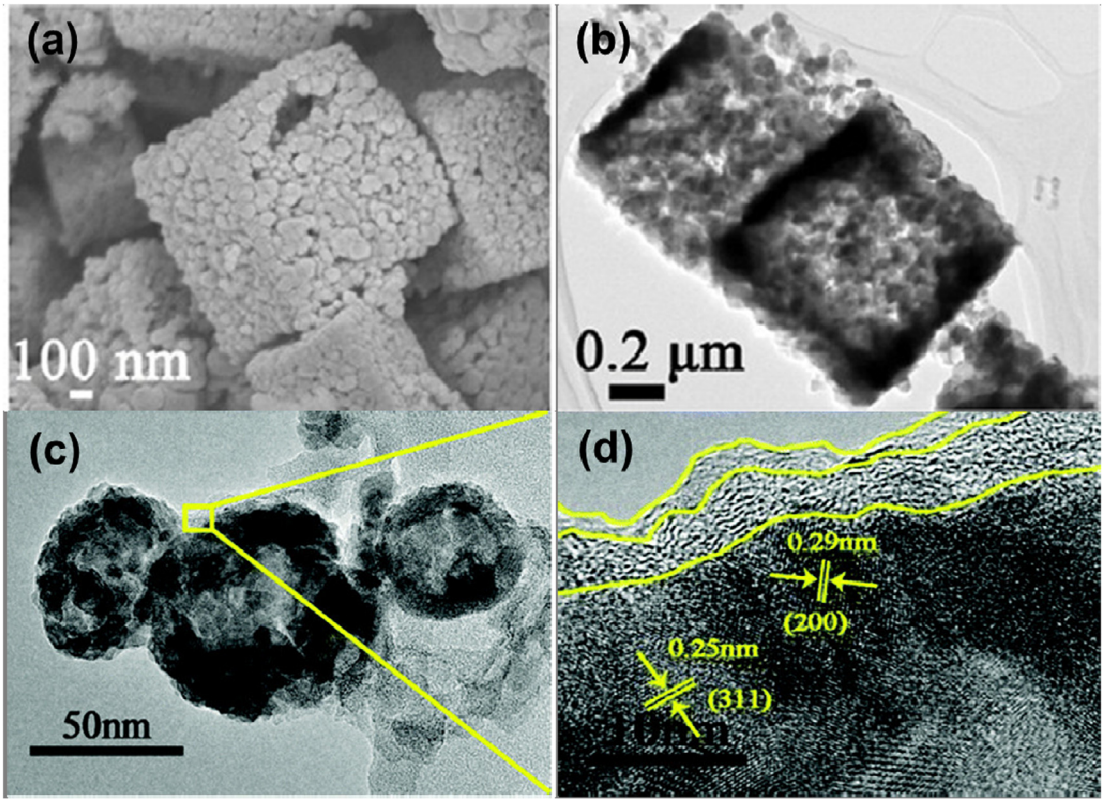

Fig. 6. (Color online) (a) FESEM image of the porous $NiFe_2O_4$ hollow cubes [34]. (b) TEM images of the porous $NiFe_2O_4$ hollow cubes [34]. (c) TEM image of the nano-hollow g-Fe_2O_3@graphene [90]. (d) Magnification of the selected region in (c) (scale bar = 10 nm) [90]. Adapted and reproduced with permission from Ref. [34] (Copyright 2015 American Chemistry Society), and Ref. [90] (Copyright 2015 Royal Society of Chemistry).

morphology of $NiFe_2O_4$ is shown in Fig. 6a and b. The hollow $NiFe_2O_4$ exhibited high specific capacities of 841 and 447 mAh g^{-1} after 100 cycles when it was tested at current densities of 1.0 and 5.0 A g^{-1}, respectively.

In order to improve the low electrical conductivity of metal oxides, nitrogen-doped carbon coated hollow Fe_3O_4 nanocages were synthesized using polydopamine as carbon and nitrogen source [91]. The N-doped carbon coated Fe_3O_4 nanocages reveal much improved cycling stability compared to that of pristine sample. RGO is also used to increase the conductivity of PBAs [90]. Core@-shell hollow Fe_2O_3@graphene hybrid was produced through a Kirkendall process and the in-situ generated graphene is closely coated on the surface of Fe_2O_3 with a thickness of ca. 3 nm (Fig. 6c and d). It demonstrates a high reversible capacity of 1095, 833, and 551 mAh g^{-1} at the current rates of 0.1, 1, and 2 C after 100 cycles, respectively. The excellent capacity should be ascribed to numerous active sites originated from PB and closely contacted graphene layers.

4. Prussian blue derivatives as catalysts for metal-air battery

Thanks to its high energy density and efficiency, metal-air batteries especially lithium-air [43,95–98] and zinc-air [28,44,45,99]

batteries have been considered as alternative promising energy storage devices. PBAs with a controlled structure have been used as a self-template to synthesize porous metal oxides [35,39] as catalysts of metal-air batteries. $Mn_3[Co(CN)_6]_2{\cdot}9H_2O$ nanoboxes were etched by NaOH solution to form hollow Mn_3O_4 nanoboxes which were further oxidized to δ-MnO_2 [43]. The obtained hollow δ-MnO_2 nanoboxes with hierarchical surface (Fig. 7a) and high surface area of 249.3 $m^2\ g^{-1}$ was demonstrated as cathode catalyst for Li-O_2 battery. The high intrinsic catalytic activity induced by the unique morphology of δ-MnO_2 nanoboxes gives rise to high capacity and reduced overpotential in Li-O_2 battery testing compared to that of pure carbon (Fig. 7b). A $Mn_xCo_{3-x}O_4$/N-Ketjenblack composite composed of a porous manganese cobalt oxide and a nitrogen-doped carbon was prepared by low temperature (400 °C) thermal decomposition of $Mn_3[Co(CN)_6]_2{\cdot}nH_2O$ and gelatin-coated Ketjenblack and shows a high catalytic activity (comparable to Pt/C) for oxygen reduction reaction (ORR) in alkaline media [44]. The pyridinic and pyrrolic N species in N-doped Ketjenblack are derived from the thermal decomposition of PBAs and behave as the active sites in ORR process [100–102]. The porous spinel oxides derived from PBAs and N species have a synergistic effect on ORR catalysis and show higher ORR activity than physical mixture of bare $Mn_xCo_{3-x}O_4$ and Ketjenblack, which are commonly observed in nanocomposites of metal nanoparticles and N-doped grapheme [103,104]. When used in a zinc-air single cell, $Mn_xCo_{3-x}O_4$/N-Ketjenblack cell has lower polarization at high current density (>200 mA cm^{-2}) than the cell catalyzed by Pt/C. The power density of $Mn_xCo_{3-x}O_4$/N-Ketjenblack cell at 0.8 V is 16% higher than that of Pt/C (Fig. 7c and d).

5. Conclusion and perspective

This review highlights the recent progress in the applications of PBAs as electrodes for mono/multivalent ion batteries and metal-air batteries. The low cost, easy preparation, unique open framework, and tunable composition/structure make PBAs suitable as cation hosts especially for large cations like sodium and potassium. In order to take PBAs into practical use, further improvements of PBAs' rate capability and cycling life are essential and it requires substantial enhancement of both ionic and electronic conductivity of PBAs. As for ionic diffusion, lithium intercalation is relatively easy in PBAs while for sodium or potassium it is more sluggish because of generally existed defects and coordinated water which hinder the sodium/potassium diffusion. By well-controlled crystallization processes, the vacancies and water contents in PBAs can be substantially decreased and thereby improving the capacity and cyclability of LIB and SIB. For multivalent cations, not only the increased size but also the increased electrostatic interaction that adversely impact on cation diffusion. In this case, increasing the amount of vacancies and coordinated water could alleviate the electrostatic force and benefit cation transport and storage. On the other hand, a meso/macroporous morphology can also provide

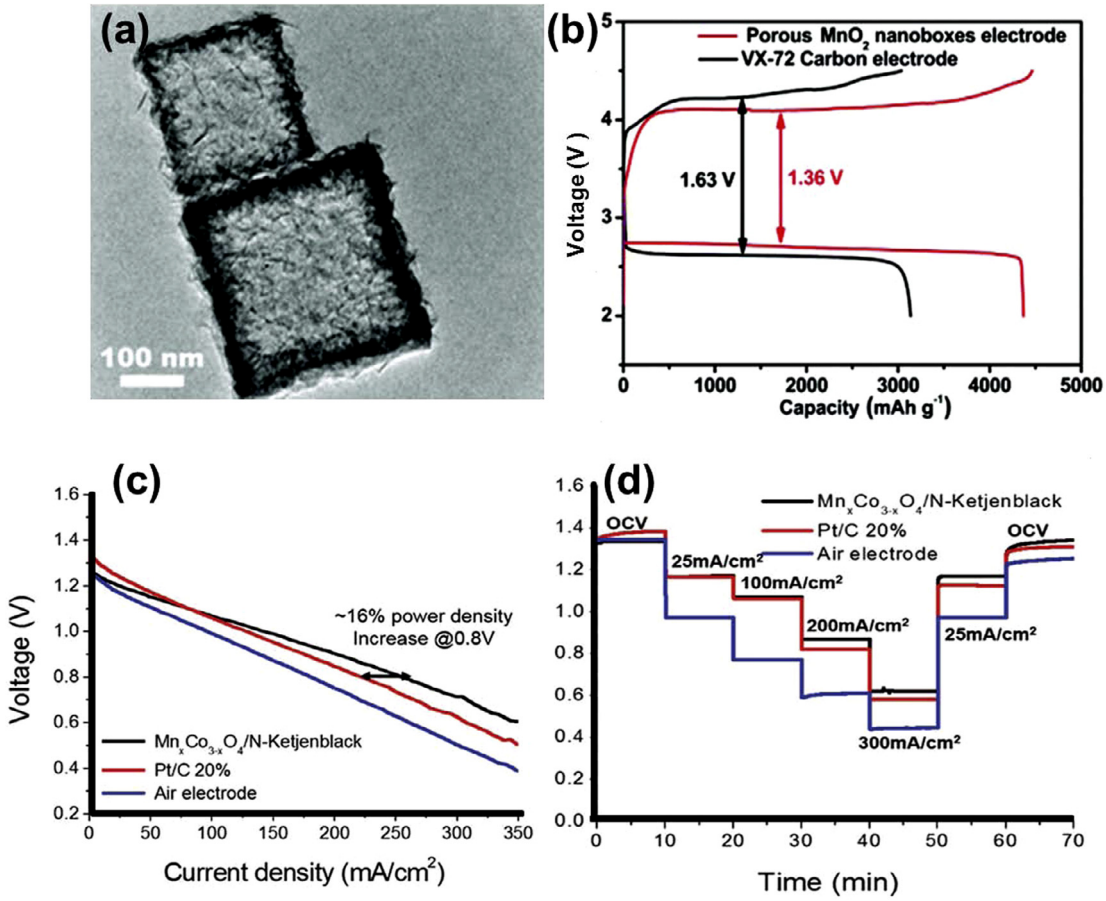

Fig. 7. (Color online) (a) TEM image of hierarchical porous δ-MnO_2 nanoboxes [43]. (b) First discharge-charge curves of Li-O_2 batteries with the hierarchical porous δ-MnO_2 nanoboxes and bare VX-72 carbon electrodes at 0.08 mA cm^{-2} [43]. (c) Current density-voltage (*J-V*) profiles of the Pt/C and porous $Mn_xCo_{3-x}O_4$/N-Ketjenblack catalyzed air electrodes and that of a bare air electrode in Zn-air batteries [44]. (d) Discharge profiles of the Zn-air batteries from low current densities to high current densities (open-circuit voltage (OCV), 25, 100, 200, and 300 mA cm^{-2}, and recovery to OCV) [44]. Adapted and reproduced with permission from Ref. [43] (Copyright 2015 Royal Society of Chemistry) and Ref. [44] (Copyright 2016 Wiley-VCH).

an easy access to electrolyte and accelerate the diffusion of cations. The low electric conductivity of PBA which drags down its electrochemical performance can be significantly improved by mixing or coating conductive carbons such as graphene, carbon nanotube, and carbon black. Moreover, the facile preparation process and composition diversity of PBAs (almost all of the first row transition metal can be incorporated into the open framework of PBA) can be fully utilized by those who want to design a multi-component metal oxide as catalysts for metal-air batteries. With all these points in mind, it is believed that the fundamental studies on PBA materials will enable the development of the practical PBA electrode materials that are highly efficient for electrochemical energy storages.

Conflict of interest

The authors declare that they have no conflict of interest.

Acknowledgments

Q. Li thanks for financial supports from the National 1000 Young Talents Program of China, the National Nature Science Foundation of China (21603078) and National Materials Genome Project (2016YFB0700600). G. Wu acknowledges the start-up funding from the University at Buffalo (Buffalo, New York, United States), The State University of New York (SUNY) along with the National Science Foundation (CBET-1511528 and 1604392), United States.

References

[1] Song LX, Yang SJ, Wei W, et al. Hierarchical SnO_2 nanoflowers assembled by atomic thickness nanosheets as anode material for lithium ion battery. Sci Bull 2015;60:892–5.
[2] Xiong JY, Han C, Li Z, et al. Effects of nanostructure on clean energy: big solutions gained from small features. Sci Bull 2015;60:2083–90.
[3] Myung S, Maglia F, Park K, et al. Nickel-rich layered cathode materials for automotive lithium-ion batteries: achievements and perspectives. ACS Energy Lett 2017;2:196–223.
[4] Lv CX, Yang XF, Umar A, et al. Architecture-controlled synthesis of M_xO_y (M = Ni, Fe, Cu) microfibres from seaweed biomass for high-performance lithium ion battery anodes. J Mater Chem A 2015;3:22708–15.
[5] Zou Y, Yang X, Lv C, et al. Multishelled Ni-Rich $Li(Ni_xCo_yMn_z)O_2$ hollow fibers with low cation mixing as high-performance cathode materials for li-ion batteries. Adv Sci 2017;4:1600262.
[6] Liu RQ, Li DY, Wang C, et al. Core-shell structured hollow SnO_2-polypyrrole nanocomposite anodes with enhanced cyclic performance for lithium-ion batteries. Nano Energy 2014;6:73–81.
[7] Wang C, Higgins D, Wang FF, et al. Controlled synthesis of micro/nanostructured cuo anodes for lithium-ion batteries. Nano Energy 2014;9:334–44.
[8] Padhi AK, Nanjundaswamy KS, Goodenough JB. Phospho-olivines as positive-electrode materials for rechargeable lithium batteries. J Electrochem Soc 1997;144:1188–94.
[9] Wang JJ, Sun XL. Olivine $LiFePO_4$: the remaining challenges for future energy storage. Energy Environ Sci 2015;8:1110–38.
[10] Kim H, Kim H, Ding Z, et al. Recent progress in electrode materials for sodium-ion batteries. Adv Mater 2016;6:1600943.
[11] Xing Z, Jian Z, Luo W, et al. A perylene anhydride crystal as a reversible electrode for k-ion batteries. Energy Storage Mater 2016;2:63–8.
[12] Zhang C, Xu Y, Zhou M, et al. Potassium prussian blue nanoparticles: a low-cost cathode material for potassium-ion batteries. Adv Funct Mater 2017;27:1604307.
[13] Mizuno Y, Okubo M, Asakura D, et al. Impedance spectroscopic study on interfacial ion transfers in cyanide-bridged coordination polymer electrode with organic electrolyte. Electrochim Acta 2012;63:139–45.
[14] Moritomo Y, Takachi M, Kurihara Y, et al. Synchrotron-radiation X-ray investigation of Li^+/Na^+ intercalation into prussian blue analogues. Adv Mater Sci Eng 2013:967285.
[15] Pramudita JC, Schmid S, Godfrey T, et al. Sodium uptake in cell construction and subsequent in operando electrode behaviour of prussian blue analogues, $Fe[Fe(CN)_6]_{(1-x)\cdot}yH_2O$ and $FeCo(CN)_6$. Phys Chem Chem Phys 2014;16:24178–87.
[16] Sun H, Sun HB, Wang W, et al. $Fe_4[Fe(CN)_6]_3$: a cathode material for sodium-ion batteries. RSC Adv 2014;4:42991–5.
[17] Wang L, Song J, Qiao RM, et al. Rhombohedral prussian white as cathode for rechargeable sodium-ion batteries. J Am Chem Soc 2015;137:2548–54.
[18] Piernas-Munoz MJ, Castillo-Martinez E, Bondarchuk O, et al. Higher voltage plateau cubic prussian white for na-ion batteries. J Power Sources 2016;324:766–73.
[19] Wang XJ, Krumeich F, Nesper R. Nanocomposite of manganese ferrocyanide and graphene: a promising cathode material for rechargeable lithium ion batteries. Electrochem Commun 2013;34:246–9.
[20] Takachi M, Fukuzumi Y, Moritomo Y. Concentration dependence of Li^+/Na^+ diffusion in manganese hexacyanoferrates. Jpn J Appl Phys 2016;55:067101.
[21] Takachi M, Matsuda T, Moritomo Y. Cobalt hexacyanoferrate as cathode material for Na^+ secondary battery. Appl Phys Express 2013;6:025802.
[22] Zhai CX, Du N, Zhang H, et al. Cobalt-iron cyanide hollow cubes: three-dimensional self-assembly and magnetic properties. J Alloy Compd 2011;509:8382–6.
[23] Lipson AL, Han SD, Kim S, et al. Nickel hexacyanoferrate, a versatile intercalation host for divalent ions from nonaqueous electrolytes. J Power Sources 2016;325:646–52.
[24] Omarova M, Koishybay A, Yesibolati N, et al. Nickel hexacyanoferrate nanoparticles as a low cost cathode material for lithium-ion batteries. Electrochim Acta 2015;184:58–63.
[25] Liu S, Pan GL, Li GR, et al. Copper hexacyanoferrate nanoparticles as cathode material for aqueous al-ion batteries. J Mater Chem A 2015;3:959–62.
[26] Majidi MR, Asadpour-Zeynali K, Shahmoradi K, et al. Electrochemical characteristics of a copper hexacyanoferrate (CuHCNF) modified composite carbon electrode and its application toward sulfite oxidation. J Chin Chem Soc 2010;57:391–8.
[27] Ni G, Han B, Li QY, et al. Instability of zinc hexacyanoferrate electrode in an aqueous environment: redox-induced phase transition, compound dissolution, and inhibition. Chemelectrochem 2016;3:798–804.
[28] Liu X, Park M, Kim MG, et al. Integrating nico alloys with their oxides as efficient bifunctional cathode catalysts for rechargeable zinc-air batteries. Angew Chem Int Ed 2015;54:9654–8.
[29] Xiao PH, Song J, Wang L, et al. Theoretical study of the structural evolution of a $Na_2FeMn(CN)_6$ cathode upon na intercalation. Chem Mater 2015;27:3763–8.
[30] Wu XY, Wu CH, Wei CX, et al. Highly crystallized $Na_2CoFe(CN)_6$ with suppressed lattice defects as superior cathode material for sodium-ion batteries. ACS Appl Mater Interfaces 2016;8:5393–9.
[31] Sottmann J, Bernal FLM, Yusenko KV, et al. In operando synchrotron xrd/xas investigation of sodium insertion into the prussian blue analogue cathode material $Na_{1.32}Mn[Fe(CN)_6]_{(0.83)\cdot}zH_2O$. Electrochim Acta 2016;200:305–13.
[32] Feng Y, Yu XY, Paik U. Formation of Co_3O_4 microframes from MOFs with enhanced electrochemical performance for lithium storage and water oxidation. Chem Commun 2016;52:6269–72.
[33] Hu L, Zhang P, Sun YK, et al. ZnO/Co_3O_4 porous nanocomposites derived from MOFs: room-temperature ferromagnetism and high catalytic oxidation of Co. ChemPhysChem 2013;14:3953–9.
[34] Yu H, Fan HS, Yadian BL, et al. General approach for MOF-derived porous spinel AFe_2O_4 hollow structures and their superior lithium storage properties. ACS Appl Mater Interfaces 2015;7:26751–7.
[35] Zhang L, Wu HB, Xu R, et al. Porous Fe_2O_3 nanocubes derived from MOFs for highly reversible lithium storage. CrystEngComm 2013;15:9332–5.
[36] Zhu DQ, Zheng FC, Xu SH, et al. MOF-derived self-assembled ZnO/Co_3O_4 nanocomposite clusters as high-performance anodes for lithium-ion batteries. Dalton Trans 2015;44:16946–52.
[37] Li Q, Pan HY, Higgins D, et al. Metal-organic framework-derived bamboo-like nitrogen-doped graphene tubes as an active matrix for hybrid oxygen-reduction electrocatalysts. Small 2015;11:1443–52.
[38] Xu YA, Wei QL, Xu C, et al. Layer-by-layer $Na_3V_2(PO_4)_3$ embedded in reduced graphene oxide as superior rate and ultralong-life sodium-ion battery cathode. Adv Energy Mater 2016;6:1600389.
[39] Hu L, Zhang P, Zhong H, et al. Foamlike porous spinel $Mn_xCo_{3-x}O_4$ material derived from $Mn_3[Co(CN)_6]_2\cdot nH_2O$ nanocubes: a highly efficient anode material for lithium batteries. Chem Eur J 2012;18:15049–56.
[40] Zhang L, Wu HB, Madhavi S, et al. Formation of Fe_2O_3 microboxes with hierarchical shell structures from metal-organic frameworks and their lithium storage properties. J Am Chem Soc 2012;134:17388–91.
[41] Zhang L, Wu HB, Lou XW. Metal-organic-frameworks-derived general formation of hollow structures with high complexity. J Am Chem Soc 2013;135:10664–72.
[42] Nie P, Shen LF, Luo HF, et al. Prussian blue analogues: a new class of anode materials for lithium ion batteries. J Mater Chem A 2014;2:5852–7.
[43] Zhang J, Luan YP, Lyu ZY, et al. Synthesis of hierarchical porous delta-MnO_2 nanoboxes as an efficient catalyst for rechargeable Li-O_2 batteries. Nanoscale 2015;7:14881–8.
[44] Lee J-S, Nam G, Sun J, et al. Composites of a prussian blue analogue and gelatin-derived nitrogen-doped carbon-supported porous spinel oxides as electrocatalysts for a Zn-air battery. Adv Energy Mater 2016:1601052.
[45] Zeng M, Liu YL, Zhao FP, et al. Metallic cobalt nanoparticles encapsulated in nitrogen-enriched graphene shells: its bifunctional electrocatalysis and application in zinc-air batteries. Adv Funct Mater 2016;26:4397–404.

[46] Imanishi N, Morikawa T, Kondo J, et al. Lithium intercalation behavior into iron cyanide complex as positive electrode of lithium secondary battery. J Power Sources 1999;79:215–9.
[47] Okubo M, Asakura D, Mizuno Y, et al. Switching redox-active sites by valence tautomerism in prussian blue analogues $A_{(x)}Mn_{(y)}Fe(CN)_{(6)}{\cdot}nH_2O$ (A: K, Rb): robust frameworks for reversible li storage. J Phys Chem Lett 2010;1:2063–71.
[48] Asakura D, Okubo M, Mizuno Y, et al. Fabrication of a cyanide-bridged coordination polymer electrode for enhanced electrochemical ion storage ability. J Phys Chem C 2012;116:8364–9.
[49] Okubo M, Honma I. Ternary metal prussian blue analogue nanoparticles as cathode materials for Li-ion batteries. Dalton Trans 2013;42:15881–4.
[50] Wong MH, Zhang ZX, Yang XF, et al. One-pot in situ redox synthesis of hexacyanoferrate/conductive polymer hybrids as lithium-ion battery cathodes. Chem Commun 2015;51:13674–7.
[51] Lu YH, Wang L, Cheng JG, et al. Prussian blue: a new framework of electrode materials for sodium batteries. Chem Commun 2012;48:6544–6.
[52] Fernandez-Ropero AJ, Piernas-Munoz MJ, Castillo-Martinez E, et al. Electrochemical characterization of $NaFe_2(CN)_6$ prussian blue as positive electrode for aqueous sodium-ion batteries. Electrochim Acta 2016;210:352–7.
[53] You Y, Wu XL, Yin YX, et al. High-quality prussian blue crystals as superior cathode materials for room-temperature sodium-ion batteries. Energy Environ Sci 2014;7:1643–7.
[54] Wu XY, Luo Y, Sun MY, et al. Low-defect prussian blue nanocubes as high capacity and long life cathodes for aqueous Na-ion batteries. Nano Energy 2015;13:117–23.
[55] Yang DZ, Xu J, Liao XZ, et al. Prussian blue without coordinated water as a superior cathode for sodium-ion batteries. Chem Commun 2015;51:8181–4.
[56] Wang L, Lu YH, Liu J, et al. A superior low-cost cathode for a Na-ion battery. Angew Chem Int Ed 2013;52:1964–7.
[57] Yang DZ, Xu J, Liao XZ, et al. Structure optimization of prussian blue analogue cathode materials for advanced sodium ion batteries. Chem Commun 2014;50:13377–80.
[58] Liu Y, Qiao Y, Zhang WX, et al. Sodium storage in Na-rich $NaFeFe(CN)_6$ nanocubes. Nano Energy 2015;12:386–93.
[59] You Y, Yu XQ, Yin YX, et al. Sodium iron hexacyanoferrate with high na content as a Na-rich cathode material for Na-ion batteries. Nano Res 2015;8:117–28.
[60] Xie M, Xu MH, Huang YX, et al. $Na_2Ni_xCo_{1-x}Fe(CN)_6$: a class of prussian blue analogs with transition metal elements as cathode materials for sodium ion batteries. Electrochem Commun 2015;59:91–4.
[61] Yu SL, Li Y, Lu YH, et al. A promising cathode material of sodium-iron nickel hexacyanoferrate for sodium ion batteries. J Power Sources 2015;275:45–9.
[62] Yue YF, Binder AJ, Guo BK, et al. Mesoporous prussian blue analogues: template-free synthesis and sodium-ion battery applications. Angew Chem Int Ed 2014;53:3134–7.
[63] Chen RJ, Huang YX, Xie M, et al. Preparation of prussian blue submicron particles with a pore structure by two-step optimization for Na-ion battery cathodes. ACS Appl Mater Interfaces 2016;8:16078–86.
[64] Jiang X, Liu H, Song J, et al. Hierarchical mesoporous octahedral $K_2Mn_{1-x}Co_xFe(CN)_6$ as a superior cathode material for sodium-ion batteries. J Mater Chem A 2016;4:16205–12.
[65] Zhang W, Zhao YY, Malgras V, et al. Synthesis of monocrystalline nanoframes of prussian blue analogues by controlled preferential etching. Angew Chem Int Ed 2016;55:8228–34.
[66] Nie P, Shen LF, Pang G, et al. Flexible metal-organic frameworks as superior cathodes for rechargeable sodium-ion batteries. J Mater Chem A 2015;3:16590–7.
[67] Prabakar SJR, Jeong J, Pyo M. Highly crystalline prussian blue/graphene composites for high-rate performance cathodes in na-ion batteries. RSC Adv 2015;5:37545–52.
[68] Jiang YZ, Yu SL, Wang BQ, et al. Prussian blue@C composite as an ultrahigh-rate and long-life sodium-ion battery cathode. Adv Funct Mater 2016;26:5315–21.
[69] You Y, Yao HR, Xin S, et al. Subzero-temperature cathode for a sodium-ion battery. Adv Mater 2016;28:7243–8.
[70] Wessells CD, Peddada SV, Huggins RA, et al. Nickel hexacyanoferrate nanoparticle electrodes for aqueous sodium and potassium ion batteries. Nano Lett 2011;11:5421–5.
[71] Wessells CD, McDowell MT, Peddada SV, et al. Tunable reaction potentials in open framework nanoparticle battery electrodes for grid-scale energy storage. ACS Nano 2012;6:1688–94.
[72] Lee J-H, Ali G, Kim DH, et al. Metal-organic framework cathodes based on a vanadium hexacyanoferrate prussian blue analogue for high-performance aqueous rechargeable batteries. Adv Energy Mater 2016:1601491.
[73] Wu XY, Sun MY, Guo SM, et al. Vacancy-free prussian blue nanocrystals with high capacity and superior cyclability for aqueous sodium-ion batteries. ChemNanoMat 2015;1:188–93.
[74] Wang RY, Wessells CD, Huggins RA, et al. Highly reversible open framework nanoscale electrodes for divalent ion batteries. Nano Lett 2013;13:5748–52.
[75] Wang RY, Shyam B, Stone KH, et al. Reversible multivalent (monovalent, divalent, trivalent) ion insertion in open framework materials. Adv Energy Mater 2015;5:1401869.
[76] Liu Z, Pulletikurthi G, Endres F. A prussian blue/zinc secondary battery with a bio-ionic liquid-water mixture as electrolyte. ACS Appl Mater Interfaces 2016;8:12158–64.
[77] Kim DM, Kim Y, Arumugam D, et al. Co-intercalation of Mg^{2+} and Na^+ in $Na_{0.69}Fe_2(CN)_6$ as a high-voltage cathode for magnesium batteries. ACS Appl Mater Interfaces 2016;8:8554–60.
[78] Shiga T, Kondo H, Kato Y, et al. Insertion of calcium ion into prussian blue analogue in nonaqueous solutions and its application to a rechargeable battery with dual carriers. J Phys Chem C 2015;119:27946–53.
[79] Yagi S, Fukuda M, Ichitsubo T, et al. EQCM analysis of redox behavior of cufe prussian blue analog in Mg battery electrolytes. J Electrochem Soc 2015;162:A2356–61.
[80] Zhang LY, Chen L, Zhou XF, et al. Morphology-dependent electrochemical performance of zinc hexacyanoferrate cathode for zinc-ion battery. Sci Rep 2015;5:18263.
[81] Sun X, Duffort V, Nazar LF. Prussian blue Mg-Li hybrid batteries. Adv Sci 2016;3:1600044.
[82] Tojo T, Sugiura Y, Inada R, et al. Reversible calcium ion batteries using a dehydrated prussian blue analogue cathode. Electrochim Acta 2016;207:22–7.
[83] Zhang H, Yu Y, Zhang L, et al. Self-powered fluorescence display devices based on a fast self-charging/recharging battery (Mg/prussian blue). Chem Sci 2016;7:6721–7.
[84] Piernas-Munoz MJ, Castillo-Martinez E, Roddatis V, et al. $K_{1-x}Fe_{2+x/3}(CN)_6{\cdot}yH_2O$, prussian blue as a displacement anode for lithium ion batteries. J Power Sources 2014;271:489–96.
[85] Xiong PX, Zeng GJ, Zeng LX, et al. Prussian blue analogues $Mn[Fe(CN)_6]_{(0.6667)}{\cdot}nH_2O$ cubes as an anode material for lithium-ion batteries. Dalton Trans 2015;44:16746–51.
[86] Hu L, Yan N, Chen QW, et al. Fabrication based on the Kirkendall effect of Co_3O_4 porous nanocages with extraordinarily high capacity for lithium storage. Chem Eur J 2012;18:8971–7.
[87] Yan N, Hu L, Li Y, et al. Co_3O_4 nanocages for high-performance anode material in lithium-ion batteries. J Phys Chem C 2012;116:7227–35.
[88] Li Z, Li B, Yin L, et al. Prussion blue-supported annealing chemical reaction route synthesized double-shelled Fe_2O_3/Co_3O_4 hollow microcubes as anode materials for lithium-ion battery. ACS Appl Mater Interfaces 2014;6:8098–107.
[89] Hou LR, Lian L, Zhang LH, et al. Self-sacrifice template fabrication of hierarchical mesoporous bi-component-active $ZnO/ZnFe_2O_4$ sub-microcubes as superior anode towards high-performance lithium-ion battery. Adv Funct Mater 2015;25:238–46.
[90] Hu J, Zheng J, Tian L, et al. A core-shell nanohollow-gamma-Fe_2O_3@graphene hybrid prepared through the Kirkendall process as a high performance anode material for lithium ion batteries. Chem Commun 2015;51:7855–8.
[91] Wang L, Wu JF, Chen YQ, et al. Hollow nitrogen-doped Fe_3O_4/carbon nanocages with hierarchical porosities as anode materials for lithium-ion batteries. Electrochim Acta 2015;186:50–7.
[92] Yang X, Tang YB, Huang X, et al. Lithium ion battery application of porous composite oxide microcubes prepared via metal-organic frameworks. J Power Sources 2015;284:109–14.
[93] Wang D, Qi XJ, Gao HY, et al. Fabricating hierarchical porous $ZnCo_2O_4$ microspheres as high-performance anode material for lithium-ion batteries. Mater Lett 2016;164:93–6.
[94] Yang X, Xue H, Yang Q, et al. Preparation of porous $ZnO/ZnFe_2O_4$ composite from metal organic frameworks and its applications for lithium ion batteries. Chem Eng J 2017;308:340–6.
[95] Ma Z, Yuan X, Li L, et al. A review of cathode materials and structures for rechargeable lithium–air batteries. Energy Environ Sci 2015;8:2144–98.
[96] Li Q, Cao R, Cho J, et al. Nanocarbon electrocatalysts for oxygen reduction in alkaline media for advanced energy conversion and storage. Adv Energy Mater 2014;4:201301415.
[97] Li Q, Cao RG, Cho J, et al. Nanostructured carbon-based cathode catalysts for nonaqueous lithium-oxygen batteries. Phys Chem Chem Phys 2014;16:13568–82.
[98] Li Q, Xu P, Gao W, et al. Graphene/graphene tube nanocomposites templated from cage-containing metal-organic frameworks for oxygen reduction in Li-O_2 batteries. Adv Mater 2014;26:1378–86.
[99] Cao RG, Thapa R, Kim H, et al. A high-performance bio-inspired catalyst for oxygen reduction. Nat Commun 2013;4:2076.
[100] Li Q, Wu G, Cullen DA, et al. Phosphate-tolerant oxygen reduction catalysts. ACS Catal 2014;4:3193–200.
[101] Li Q, Mahmood N, Zhu JH, et al. Graphene and its composites with nanoparticles for electrochemical energy applications. Nano Today 2014;9:668–83.
[102] Li Q, Wang T, Havas D, et al. High-performance direct methanol fuel cells with precious-metal-free cathode. Adv Sci 2016;3:1600140.
[103] Li Q, Sun SH. Recent advances in the organic solution phase synthesis of metal nanoparticles and their electrocatalysis for energy conversion reactions. Nano Energy 2016;29:178–97.
[104] Li Q, Zhu WL, Fu JJ, et al. Controlled assembly of Cu nanoparticles on pyridinic-N rich graphene for electrochemical reduction of CO_2 to ethylene. Nano Energy 2016;24:1–9.